

Subsurface Evolution and Persistence of Marine Heatwaves in the Northeast Pacific

H. A. Scannell¹, G. C. Johnson², L. Thompson¹, J. M. Lyman^{2,3}, S. C. Riser¹

¹School of Oceanography, University of Washington, Seattle, WA, USA.

²Pacific Marine Environmental Laboratory, NOAA, Seattle, WA, USA.

³Joint Institute for Marine and Atmospheric Research, University of Hawaii at Manoa, Honolulu, HI, USA.

Corresponding author: Hillary A. Scannell (scanh@uw.edu)

Key Points :

- Return of The Blob, with warming and freshening, hence more buoyancy.
- Summertime heatwaves, increase stratification, inhibit mixing.
- Wintertime mixing, warming penetrates the deep, provides memory.

1 **Abstract**

2 The reappearance of a northeast Pacific marine heatwave (MHW) sounded alarms in late
3 summer 2019 for a warming event on par with the 2013–2016 MHW known as The Blob.
4 Despite these two events having similar magnitudes in surface warming, differences in
5 seasonality and salinity distinguish their evolutions. We compare and contrast the ocean’s role in
6 the evolution and persistence of the 2013–2016 and 2019–2020 MHWs using mapped
7 temperature and salinity data from Argo floats. An unusual near-surface freshwater anomaly in
8 the Gulf of Alaska during 2019 increased the stability of the water column, preventing the MHW
9 from penetrating as deeply as the 2013–2016 event. This freshwater anomaly likely contributed
10 to the intensification of the MHW by increasing the near-surface buoyancy. The gradual buildup
11 of subsurface heat content throughout 2020 in the region suggests the potential for persistent
12 ecological impacts.

13

14 **Plain Language Summary**

15 Surface marine heatwaves (MHWs) are periods of prolonged and extremely warm regional sea
16 surface temperature that can negatively impact the health and productivity of marine ecosystems.
17 Using surface and subsurface ocean observations, we compare and contrast two recent MHWs to
18 show that salinity variations play an important role in the vertical distribution of temperature
19 anomalies by changing the overall stability of the water column. During the 2019–2020 MHW,
20 the near-surface waters in the Gulf of Alaska were fresher than normal, preventing warm sea
21 surface temperatures from mixing as deeply into the subsurface as in the 2013–2016 MHW. The
22 freshening in 2019 likely enhanced warming in the buoyant surface layer. As warmer
23 temperatures gradually mix downward they can persist long after the surface MHW disappears,
24 suggesting that the ocean can provide memory for long-lived MHWs. The subsurface persistence
25 of MHWs has potential ramifications for long-lasting ecological impacts.

26

27 **1 Introduction**

28 Marine heatwaves (MHWs) have become distinguishable features of northeast (NE) Pacific
29 Ocean temperature variability that disrupt the productivity of marine ecosystems and their
30 services (Smale et al., 2019). These prolonged, discrete, and anomalously warm water events
31 (Hobday et al., 2016) are most recognizable at the sea surface and are influenced by

32 anthropogenic warming (Laufkötter, et al., 2020). The effects of long-term ocean warming have
33 led to a near-doubling in the average annual count of MHW days globally since the early 20th
34 Century (Oliver et al., 2018). Although MHWs have occurred throughout the global ocean, the
35 NE Pacific has recently emerged as a hotspot for extremely persistent and large-scale events that
36 are forced by anomalous air-sea heat flux driven by remote forcing from the tropics (Di Lorenzo
37 and Mantua, 2016; Holbrook et al., 2019), in addition to long-term warming from anthropogenic
38 greenhouse forcing (Laufkötter, et al., 2020). The most remarkable NE Pacific MHWs have
39 occurred in 2013–2016 and 2019–2020, and are colloquially referred to as The Blob (Bond et al.,
40 2015) and Blob2.0 (Amaya et al., 2020) respectively (Figure 1 and Figure S1).

41
42 The magnitude of sea surface temperature (SST) anomalies associated with MHWs depends
43 critically on the seasonal evolution of the mixed-layer depth (MLD), which deepens in winter
44 and shoals in summer. If winter mixed layer MHW anomalies are present in the early spring
45 when the NE Pacific MLD shoals, they can become trapped in the subsurface during the summer
46 through detrainment. These detrained temperature anomalies are then stored in the subsurface
47 and can reemerge the following winter when the MLD deepens and re-entrains them (Alexander
48 and Deser, 1995; Alexander et al, 1999; Alexander et al., 2001). Alternatively, in the presence of
49 downward Ekman pumping from wind stress curl, for example in the North Pacific subtropical
50 gyre, detrained anomalies can subduct, where they are further isolated from the mixed layer (Qiu
51 and Huang, 1995). Here, we explore the role of detrainment and subduction in the sequestration
52 of MHW anomalies into the permanent pycnocline where they can persist for years.

53
54 The evolution of the 2013–2016 NE Pacific MHW was complex and shaped by multiple drivers.
55 Warm SST anomalies first appeared in the southern Gulf of Alaska centered on 40°N and 150°W
56 and subsequently propagated towards the coast and south into the Southern California Current
57 System near 25°N. In the Gulf of Alaska, lower rates of turbulent heat loss during the winter of
58 2013–2014 from the ocean to atmosphere and a reduction in wind-generated stirring allowed the
59 winter mixed layer to remain unseasonably warm and shallow (Bond et al., 2015). The MHW
60 moved to the south owing to local positive downward shortwave radiation anomalies and a
61 positive SST-cloud feedback over the Southern California Current System that reinforced surface
62 warming near the coast in 2014 (Zaba and Rudnick, 2016; Myers et al., 2018; Schmeisser et al.,

63 2019). Below the mixed layer, anomalously warm and salty water was detrained to denser and
64 deeper isopycnals, reaching depths of 140 m beginning in 2014 (Jackson et al., 2018). These
65 subsurface anomalies lingered through at least 2018, long after the initial onset of atmospheric
66 forcing in late 2013.

67

68 A similar situation played out during the summer of 2019 when a resurgence of Blob-like surface
69 conditions intensified in the NE Pacific. Weakened surface wind speeds, driven by atmospheric
70 teleconnections associated with SST anomalies in the Tropical Pacific, resulted in reduced
71 evaporative heat loss from the ocean to atmosphere and limited wind-driven mixing, resulting in
72 a MHW off the U.S. West Coast (Amaya et al., 2020). Increased shortwave radiation and a
73 positive SST-cloud feedback helped to maintain the MHW over an exceptionally shallow
74 summertime mixed layer (Amaya et al., 2020). Here, we show evidence for the role of salinity
75 anomalies in increasing upper ocean stability, and describe the propagation and persistence of the
76 2019–2020 NE Pacific MHW in the subsurface.

77

78 In this study, we examine the connections between surface MHWs and the subsurface structure
79 of temperature, salinity, and density by analyzing objectively mapped monthly Argo data in the
80 NE Pacific, comparing and contrasting the 2013–2016 and 2019–2020 MHWs. We characterize
81 the spatiotemporal evolution of anomalous subsurface conditions and their connection to mixed
82 layer properties from January 2004 through June 2020, and we quantify the change in water mass
83 properties and ocean heat content anomalies within and below the mixed layer. Understanding
84 the subsurface evolution and persistence of MHWs gives insight into the potential predictability
85 and reemergence of these events in the future, where a trend towards shallower summertime
86 MLDs is expected to increase the likelihood and intensity of MHWs in the North Pacific (D.J.
87 Amaya, personal communication, 2020). The persistence and potential reoccurrence of MHWs
88 could result in long-lasting impacts on the health of marine ecosystems, especially in the
89 subsurface where the effects of warming on marine life (i.e., thermal stress) can persist for years
90 (Cavole et al., 2016).

91

92 **2 Data**

93 We analyze monthly mean SST maps from the Optimum Interpolation SST version 2 (OISSTv2)
94 dataset on a 0.25° longitude by 0.25° latitude global grid from 1982 through present (Reynolds et
95 al., 2002; 2007). These SST maps are generated from a blend of satellite (Advanced Very High
96 Resolution Radiometer only), ship, buoy (both moored and drifting), and Argo float data. The
97 satellite data are interpolated to fill gaps and are bias corrected with reference to buoys to
98 account for platform differences. We use the OISSTv2 dataset as it incorporates *in situ*
99 observations, offers complete global coverage, and spans almost 40 years.

100

101 We also analyze monthly mean fields from January 2004 through June 2020 from the updated
102 Roemmich-Gilson Argo Climatology (Roemmich and Gilson, 2009; hereafter RG09) to examine
103 the vertical structure of temperature, salinity, and density anomalies associated with MHWs.
104 Argo is a global network of autonomous profiling floats that continuously measures the
105 temperature and salinity of the upper 2,000 m of the ocean. The Argo program began in 1999
106 and now consists of over 3,800 active floats and more than 2 million hydrographic profiles
107 reported thanks to a coordinated effort from dozens of countries worldwide (Jayne et al., 2017).
108 Archived and near real-time float data are made publicly available ([http://sio-](http://sio-argo.ucsd.edu/RG_Climatology.html)
109 [argo.ucsd.edu/RG_Climatology.html](http://sio-argo.ucsd.edu/RG_Climatology.html)) and are incorporated into monthly maps on a 1° longitude
110 by 1° latitude grid beginning in January 2004 when the global array had at least 1,000 floats and
111 first approached sparse global coverage (RG09). These maps are made in 58 pressure layers with
112 the shallowest centered on 2.5 dbar and the deepest on 1,975 dbar, with finer resolution near the
113 surface (e.g., spaced 10 dbar apart from 10 to 170 dbar). The 2.5 dbar monthly temperature
114 anomalies in RG09 closely track the monthly OISSTv2 anomalies in the NE Pacific, capturing
115 large scale spatial and temporal variability.

116

117 In addition to the mapped temperature and salinity vs. pressure fields from RG09, we also
118 analyze 19,697 quality-controlled Argo profiles in the NE Pacific ($35.5\text{--}51.5^\circ\text{N}$, 135.5--
119 154.5°W ; box in Figure 1) to compute the MLD from January 2004 through June 2020 using the
120 density algorithm of Holte and Talley (2009). The sampling frequency from Argo in the NE
121 Pacific ($35.5\text{--}51.5^\circ\text{N}$, $135.5\text{--}154.5^\circ\text{W}$) steadily increases from the early 2000s, achieving over
122 1,000 profiles per year starting in 2012 (Figure S2). These profiles were downloaded from one of

123 the two Argo Global Data Assembly Centers (<https://nrlgodae1.nrlmry.navy.mil/argo/argo.html>)
124 in August 2020.

125

126 **3 Analysis**

127 We define MHWs locally when SST exceeds the monthly climatological 90th percentile for at
128 least a month using monthly data from January 2004 through June 2020. Our definition for
129 MHWs is similar to that proposed in Hobday et al. (2016) with modifications in the length of the
130 climatological period and in the minimum event duration. Owing to the prominence and
131 persistence of the 2013–2016 and 2019–2020 MHWs, our definition highlights the same large-
132 scale features described in previous studies using daily data (e.g., Gentemann et al., 2017;
133 Fewings and Brown, 2019).

134

135 Before analyzing the RG09 dataset, we fit temperature and salinity at each spatial point to the
136 mean, trend, annual, and semiannual harmonics using least squares regression from January 2004
137 through June 2020. We then remove the mean, annual, and semi-annual harmonics (but not the
138 trend) to generate anomalies. Following MHW conventions (e.g., Hobday et al., 2016), we
139 choose to retain the warming trend in the analysis using a fixed climatology computed over the
140 entire record. Furthermore, the trend would not be accurately estimated over such a short period
141 and would be extremely biased by the 2013–2016 and 2019–2020 MHWs at one end of the time-
142 series. Finally, detrending would effectively remove part of the strong MHW signal that we
143 observe towards the latter end of the record. We therefore retain it. Next, we smooth the
144 anomalies and the regression coefficients with a 5-month Hanning filter and then a 6° latitude x
145 6° longitude LOESS filter to reduce mesoscale signals that are retained in the RG09 maps. We
146 then reconstruct the total smoothed *in-situ* temperature and practical salinity maps using the
147 smoothed anomalies and smoothed model coefficients. We apply the thermodynamic equation of
148 seawater (Intergovernmental Oceanographic Commission et al., 2010) to compute the absolute
149 salinity (S_A) and conservative temperature (Θ) at each space and time grid point. Using S_A and Θ ,
150 we also compute the potential density anomaly (σ_θ) with reference to 0 dbar; expressed as a
151 particular potential density minus 1000 kg m^{-3} . The potential density represents the density a
152 fluid parcel would acquire if it were brought adiabatically to the sea surface, thus eliminating the
153 density dependence on pressure. We also map the RG09 fields of S_A , Θ , and pressure (P) to a

154 vertical density coordinate, σ_θ . We compute anomalies in S_A , Θ , and P in σ_θ coordinates, as well
155 as S_A , Θ , and σ_θ in P coordinates, by removing the monthly means of these quantities across the
156 entire 198-month time series at each spatial point and for each vertical coordinate system (σ_θ and
157 P) to get the anomalies. We describe changes in S_A , Θ , and P on an isopycnal (25.4 kg m^{-3}) that
158 may outcrop during winter. When isopycnals outcrop their properties are easily modified through
159 air-sea interactions that may drive surface MHWs. Once isopycnals subduct below the mixed
160 layer, their properties are only modified through mixing, which is usually less effective than
161 direct air-sea heat and freshwater exchange.

162

163 We examine the ocean heat content anomaly (Q') within the mixed layer (10–90 dbar),
164 thermocline (100–180 dbar), and just below the thermocline (200–280 dbar). These layers of
165 equal thickness are chosen based on the vertical profiles of subsurface temperature in the NE
166 Pacific (Figure 4b). They typify the surface, pycnocline, and interior ocean in the region,
167 allowing for the distinction of the changes in Q' with depth. We define $Q' = \int \frac{1}{g} \cdot c_p \cdot \Theta' dp$,
168 where $g = 9.8 \text{ ms}^{-2}$ is the acceleration due to gravity, $c_p = 3991.8680 \text{ J kg}^{-1}\text{K}^{-1}$ is the
169 standard specific heat of seawater when using Θ , Θ' is the conservative temperature anomaly,
170 and $\int dp$ is the integral over each of these three 80-dbar thick layers.

171

172 We apply the Holt and Talley (2009) density algorithm to 19,697 Argo float profiles in the NE
173 Pacific ($35.5\text{--}51.5^\circ\text{N}$, $135.5\text{--}154.5^\circ\text{W}$; box in Figure 1) to estimate monthly MLDs from January
174 2004 through June 2020. This method searches for the depth at which the density increases by
175 0.03 kg m^{-3} relative to a near-surface reference level.

176

177 We quantify the bulk stratification of the upper ocean using the Brunt-Väisälä frequency squared
178 $N^2 = -\frac{g}{\rho} \frac{d\rho}{dz}$. Here, $\frac{d\rho}{dz}$ is the change in potential density with reference to 0 dbar between 2.5 and
179 200 dbar. Larger values of N^2 correspond to greater upper ocean stratification — a more stable
180 water column. We compute anomalies in N^2 , again with respect to monthly long-term means, to
181 quantify the change in the stratification of the upper ocean due to MHW variations in both Θ and
182 S_A .

183

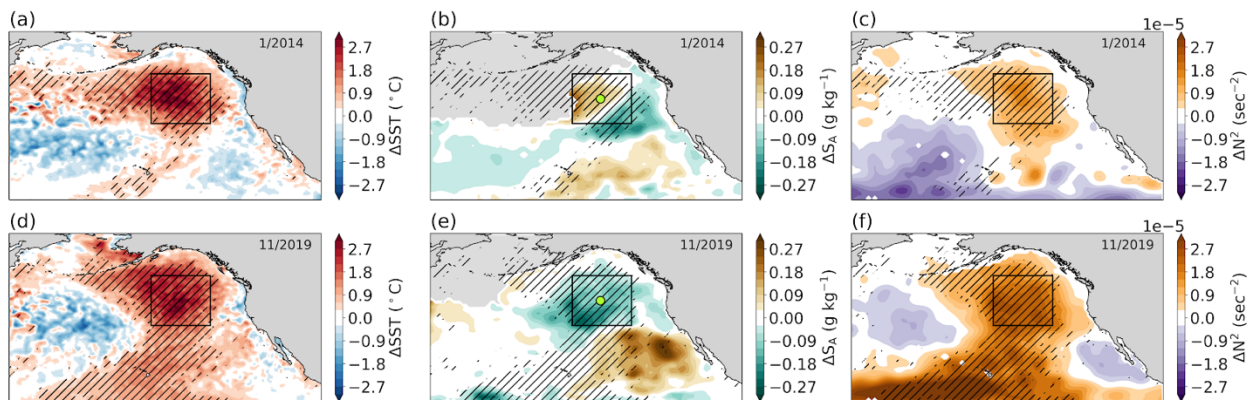
184 To further examine the relationships among Θ , S_A , and σ_θ , we examine $\Theta - S_A$ diagrams with
 185 contours of constant density and spice to show changes in water-mass properties between
 186 different MHW years in the NE Pacific. $\Theta - S_A$ variations along isopycnals can be quantified by
 187 spice (Munk, 1981), where warm/salty anomalies are spicy and cool/fresh anomalies are minty.
 188 We compute spice following McDougall and Krzysik (2015) using a potential density with
 189 reference to 0 dbar. Isopycnal variations in spiciness can be used to describe MHW impacts on
 190 isopycnal water-mass properties in density units.

191

192 4 Results

193 Anomalies in $\Theta - S_A$ on isopycnals can be tracked following the surface evolution of SST
 194 anomalies during MHWs, and can either be warm/salty (spicy) or cool/fresh (minty), such that
 195 the density of that isopycnal does not change (Movie S1). The winter-intensified 2013–2016
 196 MHW had spicy anomalies on 25.4 kg m^{-3} , which lagged the spatiotemporal evolution of SST
 197 anomalies within the MHW (Movie S1, hatching in Figure 1). For example, surface MHW
 198 conditions moved onshore by late 2014 and began to fade as early as 2015, whereas subsurface
 199 spice anomalies did not reach the coast until winter 2015 and persisted into 2016 (Movie S1). By
 200 comparison, summer $\Theta - S_A$ anomalies in 2019 lacked the advective nature of the 2013–2016
 201 MHW, yet they were much more widespread. Minty anomalies on 25.4 kg m^{-3} encompassed
 202 nearly the entire Gulf of Alaska from late summer 2018 through summer 2020, while spicy
 203 anomalies lingered off the coast between Baja California and Hawai'i (Figure 1, Movie S1).

204



205

206 **Figure 1.** Spatial characteristics of NE Pacific MHWs during January 2014 (a-c) and November
 207 2019 (d-f); the two warmest months of SST anomalies averaged in the boxed region from 2004

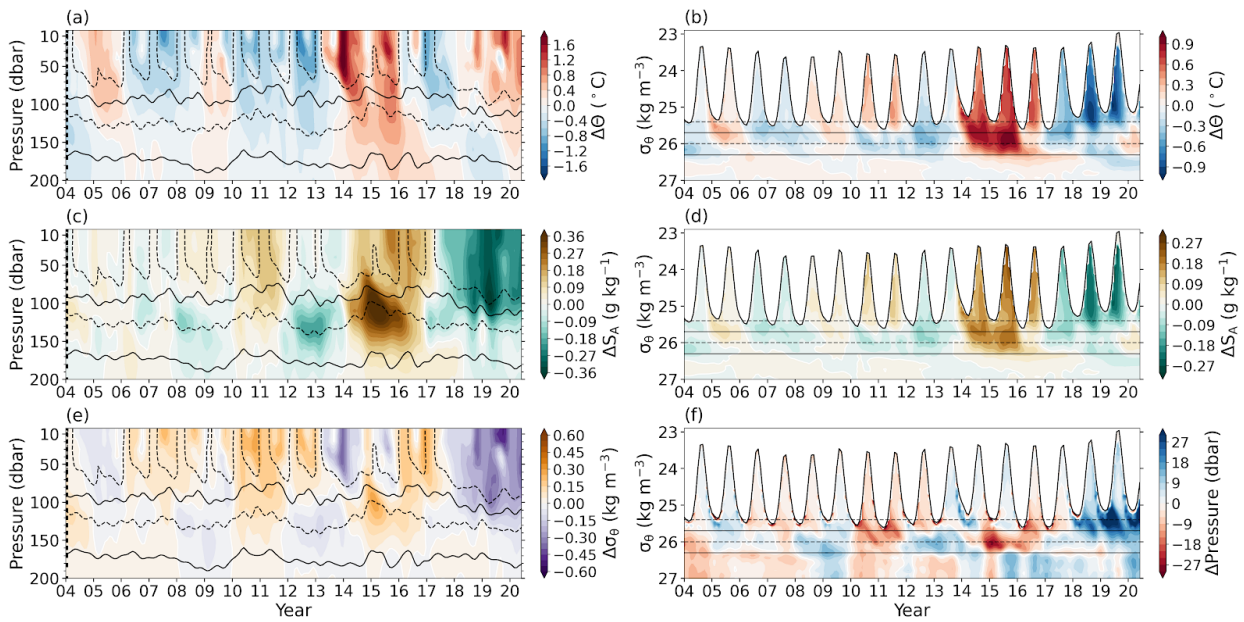
208 through 2020. First column (a,d) shows SST anomalies from the OISSTv2 where diagonal
209 hatching indicates the locations experiencing a MHW. Hatching across columns is consistent.
210 The middle column (b,d) is the absolute salinity anomaly on 25.4 kg m^{-3} . By definition,
211 conservative temperature anomalies mirror salinity anomalies on isopycnals where conditions are
212 either warm/salty or cool/fresh. The third column (c,f) shows the bulk upper ocean stability
213 anomaly in terms of the Brunt-Väisälä frequency squared computed using the anomalous density
214 difference between 2.5 and 200 dbar. All anomalies are referenced to the January 2004 through
215 June 2020 monthly climatology. The bounding black box represents the area defined by 35.5 –
216 51.5°N , 135.5 – 154.5°W and the lime green circles in (b) and (c) mark 43.5°N , 145.5°W . Gray
217 shading in panels b, c, e, and f (excluding land) shows the locations where 25.4 kg m^{-3} outcrops
218 in January 2014 (b,c) and November 2019 (e,f).

219
220 Positive stratification (N^2) anomalies occurred for both the 2013–2016 and 2019–2020 MHWs,
221 however they were much greater in 2019 (Figure 1, Movie S1). Warm and fresh near-surface
222 anomalies in 2019 decreased density and increased the stratification (Figure 2), whereas in 2013–
223 2016 the near-surface density reduction from a warm anomaly was partially offset by a salty
224 anomaly. The increase in pressure along 25.4 kg m^{-3} beginning in 2018 reflects an increase in
225 stratification even before the onset of the 2019 MHW (Figure 2). The 2019 large and positive
226 stratification anomaly likely inhibited the surface MHW from penetrating as deeply as the 2013–
227 2016 MHW, and furthermore may have enhanced the surface build-up of heat.

228
229 Prior to 2013, two other noteworthy MHWs occurred in the NE Pacific from 2004–2005 and
230 2008–2009 (Figure 2). Warm subsurface Θ anomalies during these MHWs extended and
231 propagated to depths beyond 100 dbar and anomalies at 25.4 kg m^{-3} were spicy, similar to that of
232 the 2013–2016 event (Figure 2). Warm and salty anomalies reduced subsurface density and
233 increased the stratification of the surface layer. The 2004–2005 MHW was more stratified than
234 the 2008–2009 event owing to the larger surface density anomaly (Figure 2e and Figure 5b-c).

235
236 The simultaneous change in temperature from 0–200 dbar in 2008–2009 could have resulted
237 from isopycnal heave, as indicated by the downward deflection of 26.3 kg m^{-3} (Figure 2a). Heave
238 can occur in response to Ekman pumping due to wind stress curl that depresses the main

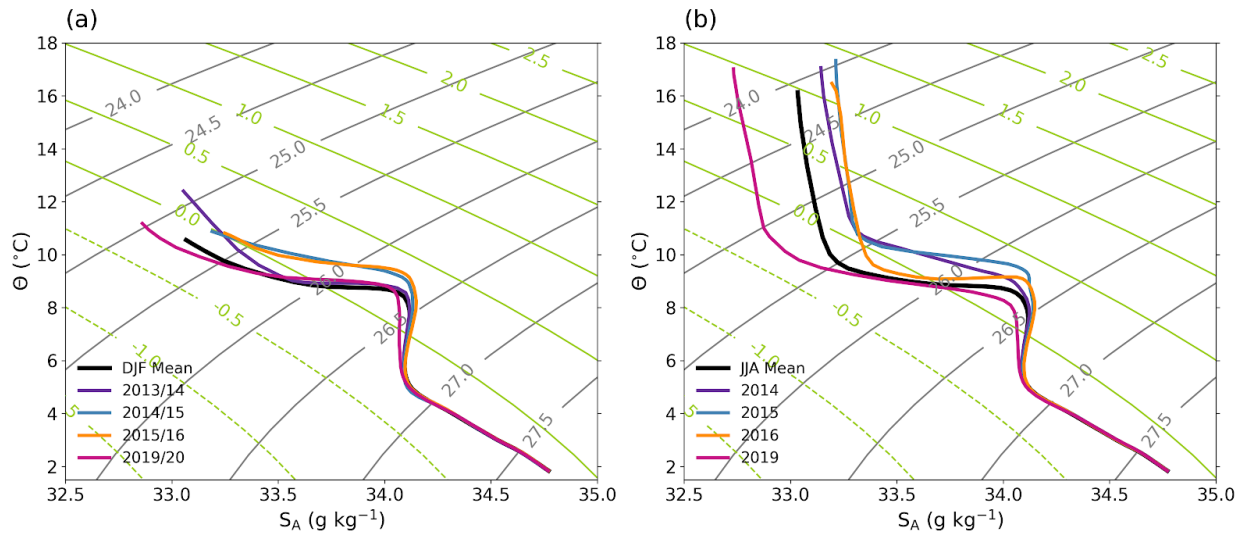
239 thermocline (Bindoff and McDougall, 1994), or from other dynamic features such as large-scale
 240 Rossby waves (Xie et al., 2016) or eddies (Pegliasco et al., 2015). Positive pressure anomalies on
 241 26 kg m^{-3} indicates a deepening of the thermocline in 2008–2009 at approximately 130 dbar
 242 (Figure 2f). These vertical isopycnal motions are nearly adiabatic. As seen from the conservation
 243 of water mass properties on the isopycnal (Figure 2b,d), there is little exchange of heat or salinity
 244 with the surrounding environment. As a result, warm and fresh anomalies in 2008–2009 occurred
 245 along the 150–200 isobars, however, were negligible on 26.3 kg m^{-3} , which ranges from 150–200
 246 dbar (Figure 2).



247
 248 **Figure 2.** Progression of monthly anomalies in (a,b) conservative temperature, (c,d) absolute
 249 salinity, (e) potential density, and (f) isopycnal pressures at 43.5°N , 145.5°W (lime green circles
 250 in Figure 1) from January 2004 through June 2020. Contours of the 25.4 kg m^{-3} (upper dashed),
 251 25.7 kg m^{-3} (upper solid), 26 kg m^{-3} (lower dashed), and 26.3 kg m^{-3} (lower solid) isopycnal
 252 surfaces vary with pressure (a,c,e), however are constant when plotted against density (b,d,f).

253
 254 Analysis of $\Theta - S_A$ relationships along isopycnals provides additional insight into water-mass
 255 property changes during MHWs. Here, spice is primarily controlled by the exchange of heat and
 256 freshwater between the ocean and atmosphere, ocean turbulent mixing, and lateral advection.
 257 Spicy conditions occurred each winter (December-January-February) during the 2013–2016
 258 MHW, most notably in waters lighter than 26.5 kg m^{-3} during the winters of 2014/15 and

259 2015/16 (Figure 3a). The warmest wintertime temperatures occurred in 2013/14 where $\Theta - S_A$
 260 variations were confined to lighter isopycnals ($<26 \text{ kg m}^{-3}$). Winter spice anomalies in 2013/14
 261 likely mixed to denser isopycnals in the permanent halocline by summer, as can be seen along
 262 25.6 kg m^{-3} during the summers of 2014 and 2015 (Figure 3b). By summer 2016, spice
 263 anomalies within the permanent halocline returned to near normal, however the seasonal
 264 thermocline remained anomalously warm and salty. Spice anomalies during the summer 2019
 265 MHW were minty compared to average. Minty conditions in June-July-August of 2019 were
 266 greatest within the seasonal thermocline above 25.5 kg m^{-3} (Figure 3b). As a consequence, the
 267 near surface $\Theta - S_A$ properties were much lighter compared to 2014–2016, both in winter and
 268 summer seasons. Minty conditions persisted into the winter of 2019/20.
 269



270
 271 **Figure 3.** Winter (December-January-February) (a) and summer (June-July-August) (b)
 272 temperature-salinity relationships at 43.5°N , 145.5°W (lime green circles in **Figure 1**). The
 273 average 2004–2019 DJF and 2004–2019 JJA curves are shown by the thick black lines. Contours
 274 of constant spice (kg m^{-3}) in green are perpendicular to isopycnals in gray.

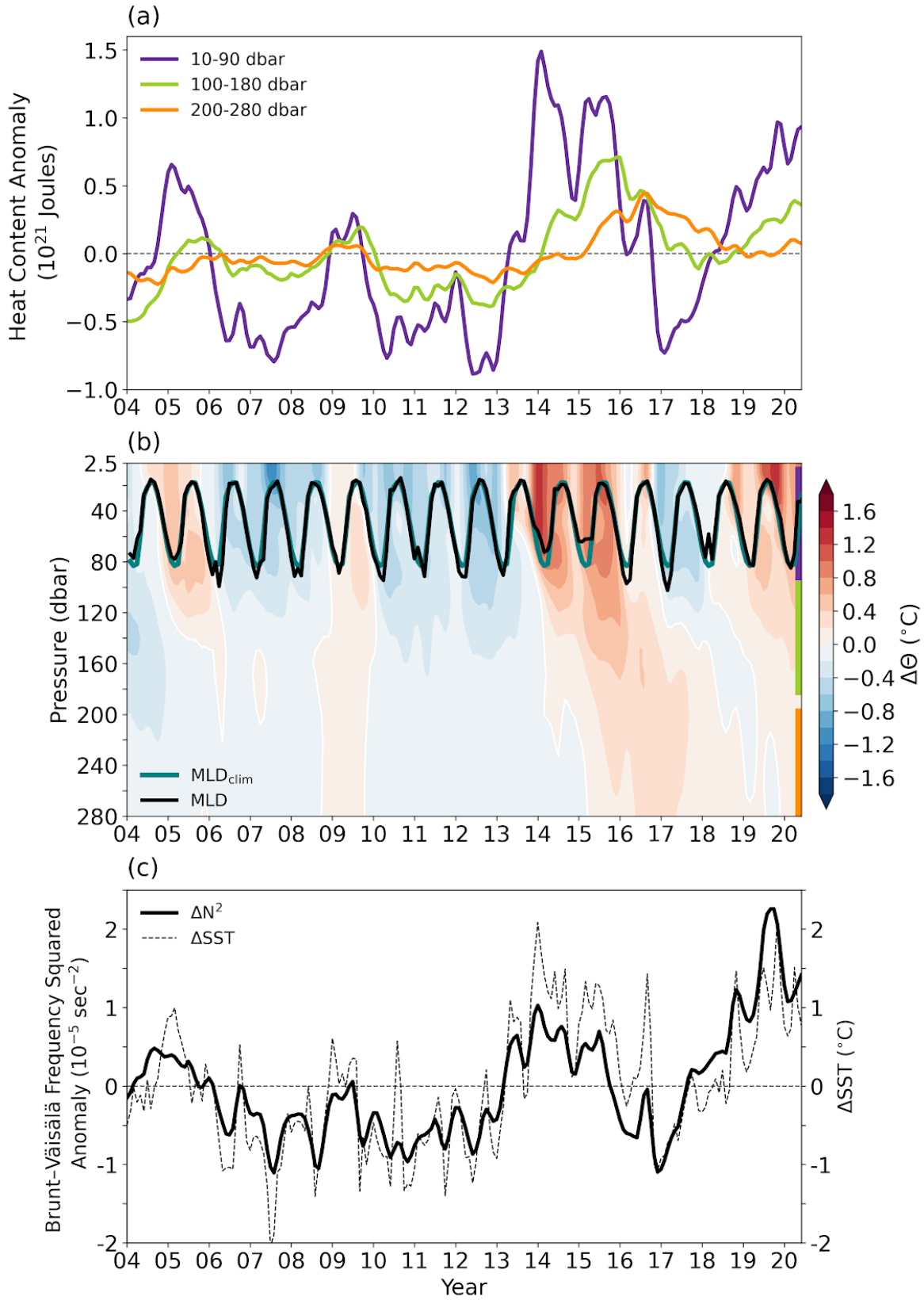
275
 276 A connection between the evolution of surface and subsurface anomalies was a recurring theme
 277 during recent 2013–2016 and 2019–2020 NE Pacific MHWs and is visible in both Figures 2 and
 278 4. To quantify the time lags associated with the penetrations of surface anomalies into the
 279 subsurface, we compute the lagged cross-correlation for Θ and S_A on isobars and isopycnals with
 280 values at 2.5 dbar and 25.7 kg m^{-3} respectively. Significant positive correlations between surface

281 and subsurface $\Theta - S_A$ anomalies increase with positive lag and density between $25.7\text{--}27 \text{ kg m}^{-3}$.
282 For example, the maximum cross-correlation on 26.3 kg m^{-3} occurs at 6 months positive lag
283 (Figure S3). On the other hand, subsurface anomalies (between 150–220 dbar) are most strongly
284 correlated with the surface conditions for positive lags of 1–2 years, while subsurface SA
285 correlations peak at 6–12 months positive lags (Figure S3 and Figure S4).

286

287 The downward progression of surface Θ and S_A anomalies suggest that the North Pacific Ocean
288 is capable of maintaining long-term memory of surface MHWs. One measure of memory is the
289 heat content anomaly, Q' , evaluated here over equal thickness subsurface layers. The largest Q'
290 values occur within the seasonally varying mixed layer (10–90 dbar) where temperature
291 fluctuations are the strongest (Figure 4). The largest positive anomalies are present during the
292 2013–2016 MHW. After a period of strong cooling, Q' steadily increased beginning in 2018
293 through present. Prior to 2013 there were two smaller MHWs that occurred in 2004–2005 and
294 2008–2009 that also had small gains of heat content. Evaluating Q' over layers spanning the
295 pycnocline (100–180 dbar) and interior (200–280 dbar) reveals the persistence of Θ anomalies
296 below the surface temperature variability. Once $\Theta - S_A$ anomalies get into the subsurface, their
297 properties are nearly conserved even after the surface cools (Figure 4).

298



300 **Figure 4.** Variations in (a) upper ocean heat content anomalies, (b) temperature anomalies and
301 mixed layer pressure, and (c) upper ocean stratification anomalies averaged in 35.5–51.5°N,
302 135.5–154.5°W (black outline in Figure 1). Ocean heat content anomalies are computed over
303 three different 80-dbar pressure layers between 10–90 dbar, 100–180 dbar, and 200–280 dbar.
304 These intervals are shown in (b) as vertical colored lines on the right-hand side corresponding to
305 (a). The mixed layer pressure and 2004-2019 climatology is computed from 19,697 Argo profiles
306 using the Holt and Talley (2009) density algorithm. The bulk upper ocean stratification anomaly
307 (solid lines) in (c) is computed as N^2 between 2.5 and 200 dbar and shown with the SST
308 anomaly (dashed lines). Positive values of N^2 indicate higher water column stability and greater
309 resistance to overturning or vertical displacement.

310
311 An increase in upper ocean heat content can affect the stability of the upper ocean. The depth of
312 the mixed layer also shoals, which can be seen during the winters of 2013/2014 and 2014/2015
313 (Figure 4). The increase in stratification reduces entrainment of cool water from below and can
314 exacerbate warming by reducing the thickness of the surface layer that accepts heat from the
315 atmosphere, making the surface ocean easier to warm. The upper ocean stratification anomaly
316 was noticeably higher (large N^2 anomaly values) in 2014–2015, with the largest values occurring
317 in 2019 (Figure 4c). The very high values in 2019–2020 arise from the anomalously fresh near-
318 surface conditions during that MHW.

319

320 **5 Discussion**

321 This study examines 21st Century MHWs in the NE Pacific based on gridded SST data, and also
322 the evolution of subsurface $\Theta - S_A$ anomalies from Argo on both isobars and isopycnals during
323 the 2013–2016 and 2019–2020 NE Pacific MHWs. Upper ocean salinity was anomalously fresh
324 in the Gulf of Alaska during the 2019–2020 MHW, which greatly increased the buoyancy of the
325 surface layer. Indeed, there was a net freshwater input from precipitation as can be seen in the
326 2018 precipitation anomaly in the Gulf of Alaska (Yu et al., 2019) that likely contributed to the
327 decrease in surface salinity (Reagan et al., 2019). The resulting increase in stratification during
328 2019–2020 likely contributed to the decrease in the depth (and density) to which water property
329 anomalies from this event were detrained, and in places subducted. The confinement of warm
330 anomalies to the near-surface likely enhanced the MHW's intensity.

331
332 There are several dynamical pathways by which surface MHW anomalies in the NE Pacific
333 could reach the subsurface; by means of detrainment, diabatic subduction (Jackson et al., 2018),
334 lateral advection (Chao et al., 2017; Zaba et al., 2020), and/or diabatic isopycnal heave.
335 Subduction occurs in subtropical regions after temperature anomalies within the deep wintertime
336 mixed layer detrain as a result of the mixed layer retreating in late spring. During the 2014 and
337 2015 spring transition of the mixed layer depth, subsurface warming occurred along both
338 isopycnals and isobars below the mixed layer, suggesting that diabatic vertical or horizontal
339 mixing could play a role in the penetration of MHW anomalies within the seasonal pycnocline.
340 Indeed, Zaba et al. (2020) attribute positive subsurface heat content anomalies within the
341 California Undercurrent to an increase in poleward heat transport from the tropics in September
342 2015. Alternatively, subsurface warming that occurs primarily on isobars and not on isopycnals
343 was likely the result of isopycnal heave, defined as the downward deflection of a potential
344 density surface. We speculate that heave is most likely responsible for the near-simultaneous
345 appearance of anomalies below 150 dbar, for example during the 2008–2009 MHW, however the
346 exact mechanisms of heave (i.e., from Ekman pumping due to wind stress curl) are not
347 investigated here.

348
349 Once surface MHW anomalies are detrained out of the deep wintertime mixed layer, they may
350 propagate downward. The lag associated with the vertical propagation of surface anomalies
351 causes the subsurface heat content to remain anomalously high even after surface conditions
352 return to normal. This persistence of subsurface heat and the possible seasonal reemergence of
353 surface anomalies could in fact help supercharge the occurrence of multi-year events. As future
354 warming trends favor a more stratified upper ocean (Li et al., 2020), we expect that detrainment
355 out of the mixed layer may become less effective in storing MHW anomalies in the subsurface,
356 and therefore further amplify surface warming. This possibility is concerning owing to the
357 impacts that accumulated heat stress and stratification have on pelagic marine ecosystems and
358 primary production (Cavole et al., 2016; Jacox et al., 2016; Smale et al, 2019).

359
360 Mixed layer heat budgets are frequently used to diagnose the drivers of surface warming
361 associated with MHWs; however, the influence of salinity and subsurface water mass properties

362 are often overlooked (Holbrook et al., 2020). Using the global Argo array data, this study
363 motivates complementary analyses on the role of salinity and subsurface $\Theta - S_A$ anomalies to
364 better understand the ocean's role in the persistence and evolution of long-lived events. Further
365 investigation into the drivers of salinity anomalies and their role in the development of NE
366 Pacific MHWs would appear to be a fruitful avenue of future research. Analysis of the full 4-D
367 heat budget using high resolution numerical models could be undertaken to investigate the local
368 mechanisms of subsurface warming.

369

370 **Acknowledgments and Data Availability**

371 HAS and LT are supported by an AI for Earth Innovation Grant sponsored by the Leonardo
372 DiCaprio Foundation and Microsoft, and wish to acknowledge cloud resources from an Azure
373 compute grant awarded through Microsoft's AI for Earth. GCJ and JML are supported by NOAA
374 Research and NOAA's Global Ocean Monitoring and Observing Program. HAS and SCR were
375 also partially supported by NOAA via grant NA15OAR4320063 to the University of Washington
376 through the Joint Institute for the Study of the Atmosphere and Ocean. This is PMEL
377 Contribution Number 5140. The NOAA OISSTv2 dataset was provided by the
378 NOAA/OAR/ESRL PSL, Boulder, Colorado, USA, from their Web site at <https://psl.noaa.gov/>.
379 Argo data were collected and made freely available by the International Argo Program and the
380 national programs that contribute to it (<http://www.argo.ucsd.edu> and <http://argo.jcommops.org>).
381 The Argo Program is part of the Global Ocean Observing System. Lastly, we would like to thank
382 two anonymous reviewers whose comments helped to improve this manuscript.

383

384 **References**

385 Alexander, M. A., & Deser, C. (1995), A Mechanism for the Recurrence of Wintertime
386 Midlatitude SST Anomalies. *Journal of Physical Oceanography*, 25, 122–137,
387 [https://doi.org/10.1175/1520-0485\(1995\)025<0122:AMFTRO>2.0.CO;2](https://doi.org/10.1175/1520-0485(1995)025<0122:AMFTRO>2.0.CO;2)

388

389 Alexander, M. A., Deser, C., & Timlin, M. S. (1999), The Reemergence of SST Anomalies in
390 the North Pacific Ocean. *Journal of Climate*, 12, 2419–2433, [https://doi.org/10.1175/1520-0442\(1999\)012<2419:TROSAI>2.0.CO;2](https://doi.org/10.1175/1520-0442(1999)012<2419:TROSAI>2.0.CO;2)

392

393 Alexander, M. A., Timlin, M. S., & Scott, J. D. (2001), Winter-to-winter recurrence of sea
394 surface temperature, salinity and mixed layer depth anomalies, *Progress in Oceanography*, 49,
395 41-6, [https://doi.org/10.1016/S0079-6611\(01\)00015-5](https://doi.org/10.1016/S0079-6611(01)00015-5)
396

397 Amaya, D. J., A. J. Miller, S. Xie, & Kosaka, Y. (2020), Physical drivers of the summer 2019
398 North Pacific marine heatwave. *Nature Communications*, 11, 1903.
399 <https://doi.org/10.1038/s41467-020-15820-w>
400

401 Bindoff, N. L., & McDougall, T. J. (1994), Diagnosing Climate Change and Ocean Ventilation
402 Using Hydrographic Data, *Journal of Physical Oceanography*, 24, 1137-1152,
403 [https://doi.org/10.1175/1520-0485\(1994\)024<1137:DCCAOV>2.0.CO;2](https://doi.org/10.1175/1520-0485(1994)024<1137:DCCAOV>2.0.CO;2)
404

405 Bond, N. A., Cronin, M. F., Freeland, H., & Mantua, N. (2015), Causes and impacts of the 2014
406 warm anomaly in the NE Pacific. *Geophysical Research Letters*, 42(9), 3414-3420.
407 <https://doi.org/10.1002/2015GL063306>
408

409 Cavole, L. M., Demko, A. M., Diner, R. E., Giddings, A., Koester, I., Pagniello, C. M. L. S.,
410 Paulsen, M. -L., Ramirez-Valdez, A., Schwenck, S. M., Yen, N. K., Zill, M. E., & Franks, P. J.
411 S. (2016), Biological impacts of the 2013–2015 warm-water anomaly in the Northeast Pacific:
412 Winners, losers, and the future. *Oceanography*, 29(2), 273–285,
413 <https://doi.org/10.5670/oceanog.2016.32>
414

415 Chao, Y., Farrara, J. D., Bjorkstedt, E., Chai, F., Chavez, F., Rudnick, D. L., Enright, W., Fisher,
416 J. L., Peterson, W. T., Welch, G. F., Davis, C. O., Dugdale, R. C., Wilkerson, F. P., Zhang, H.,
417 Zhang, Y., & Ateljevich, E. (2017), The origins of the anomalous warming in the California
418 coastal ocean and San Francisco Bay during 2014–2016, *Journal of Geophysical Research*
419 *Oceans*, 122, 7537– 7557, <https://doi.org/10.1002/2017JC013120>.
420

421 Di Lorenzo, E., & Mantua, N. (2016), Multi-year persistence of the 2014/15 North Pacific
422 marine heatwave. *Nature Climate Change*, 6, 1042-1047. <https://doi.org/10.1038/nclimate3082>
423

424 Fewings, M. R. & Brown, K. S. (2019), Regional Structure in the Marine Heat Wave of Summer
425 2015 Off the Western United States. *Frontiers in Marine Science*, 6, 564.
426 <https://doi.org/10.3389/fmars.2019.00564>
427

428 Gentemann, C. L., Fewings, M. R. & García-Reyes, M. (2017), Satellite sea surface
429 temperatures along the West Coast of the United States during the 2014–2016 northeast Pacific
430 marine heat wave. *Geophysical Research Letters*, 44, 312–319, [https://doi.org/](https://doi.org/10.1002/2016GL071039)
431 <https://doi.org/10.1002/2016GL071039>
432

433 Hobday, A. J., Alexander, L. V., Perkins, S. E., Smale, D. A., Straub, S. C., Oliver, E. C. J.,
434 Benthuyesen, J. A., Burrows, M. T., Donat, M. G., Feng, M., Holbrook, N. J., Moore, P. J.,
435 Scannell, H. A., Sen Gupta, A., & Wernberg, T. (2016), A hierarchical approach to defining
436 marine heatwaves. *Progress in Oceanography*, 141, 227-238.
437 <https://doi.org/10.1016/j.pocean.2015.12.014>
438

439 Holbrook, N. J., Scannell, H. A., Sen Gupta, A., Benthuyesen, J. A., Feng, M., Oliver, E. C. J.,
440 Alexander, L. V., Burrows, M. T., Donat, M. G., Hobday, A. J., Moore, P. J., Perkins-
441 Kirkpatrick, S. E., Smale, D. A., Straub, S. C., & Wernberg, T. (2019), A global assessment of
442 marine heatwaves and their drivers. *Nature Communications*, 10, 2624.
443 <https://doi.org/10.1038/s41467-019-10206-z>
444

445 Holbrook, N. J., Sen Gupta, A., Oliver, E. C. J., Hobday, A. J., Benthuyesen, J. A., Scannell, H.
446 A., Smale, D. A., & Wernberg, T. (2020), Keeping pace with marine heatwaves, *Nature Reviews*
447 *Earth & Environment*, <https://doi.org/10.1038/s43017-020-0068-4>
448

449 Holte, J. & Talley, L. (2009), A New Algorithm for Finding Mixed Layer Depths with
450 Applications to Argo Data and Subantarctic Mode Water Formation. *Journal of Atmospheric and*
451 *Oceanic Technology*, 26, 1920–1939. <https://doi.org/10.1175/2009JTECHO543.1>
452

453 Intergovernmental Oceanographic Commission, SCOR, and IAPSO (2010), The international
454 thermodynamic equation of seawater – 2010: Calculation and use of thermodynamic properties,
455 Intergovernmental Oceanographic Commission, Manuals and Guides No. 56, 196 pp., UNESCO
456

457 Jackson, J. M., Johnson, G. C., Dosser, H. V., & Ross, T. (2018), Warming from recent marine
458 heatwave lingers in deep British Columbia fjord. *Geophysical Research Letters*, 45, 9757– 9764.
459 <https://doi.org/10.1029/2018GL078971>
460

461 Jacox, M. G., Hazen, E. L., Zaba, K. D., Rudnick, D. L., Edwards, C. A., Moore, A. M. &
462 Bograd, S. J. (2016), Impacts of the 2015–2016 El Niño on the California Current System: Early
463 assessment and comparison to past events, *Geophysical Research Letters*, 43, 7072-7080,
464 <https://doi.org/10.1002/2016GL069716>
465

466 Jayne, S.R., Roemmich, D., Zilberman, N., Riser, S. C., Johnson, K. S., Johnson, G. C., &
467 Piotrowicz, S. R. (2017), The Argo Program: Present and future. *Oceanography*, 30(2), 18–28.
468 <https://doi.org/10.5670/oceanog.2017.213>
469

470 Laufkötter, C., Zscheischler, J., & Frölicher, T. L. (2020). High-impact marine heatwaves
471 attributable to human-induced global warming, *Science*, 369(6511), 1621-1625.
472 <https://doi.org/10.1126/science.aba0690>
473

474 Li, G., Cheng, L., Zhu, J., Trenberth, K. E., Mann, M. E., & Abraham, J. P. (2020). Increasing
475 ocean stratification over the past half-century. *Nature Climate Change*,
476 <https://doi.org/10.1038/s41558-020-00918-2>
477

478 McDougall, T. J., & Krzysik, O. A. (2015), Spiciness, *Journal of Marine Research*, 73, 141-
479 152, <https://doi.org/10.1357/002224015816665589>
480

481 Munk, W., 1981: Internal waves and small-scale processes. *Evolution of Physical*
482 *Oceanography*, B. A. Warren and C. Wunsch, Eds., MIT Press, 264–291
483

484 Myers, T. A., Mechoso, C. R., Cesana, G. V., DeFlorio, M. J., & Waliser, D. E. (2018), Cloud
485 feedback key to marine heatwave off Baja California. *Geophysical Research Letters*, 45, 4345–
486 4352, <https://doi.org/10.1029/2018GL078242>
487

488 Oliver, E. C. J., Donat, M. G., Burrows, M. T., Moore, P. J., Smale, D. A., Alexander, L. V.,
489 Benthuisen, J. A., Feng, M., Sen Gupta, A., Hobday, A. J., Holbrook, N. J., Perkins-Kirkpatrick,
490 S. E., Scannell, H. A., Straub, S. C. & Wernberg, T. (2018), Longer and more frequent marine
491 heatwaves over the past century, *Nature Communications*, 9, 1324,
492 <https://doi.org/10.1038/s41467-018-03732-9>
493

494 Pegliasco, C., Chaigneau, A., & Morrow, R. (2015), Main eddy vertical structures observed in
495 the four major Eastern Boundary Upwelling Systems, *Journal of Geophysical Research Oceans*,
496 120, 6008– 6033, <https://doi.org/10.1002/2015JC010950>
497

498 Qiu, B., & Huang, R. X. (1995), Ventilation of the North Atlantic and North Pacific:
499 Subductions Versus Obduction, *Journal of Physical Oceanography*, 25, 2374-2390,
500 [https://doi.org/10.1175/1520-0485\(1995\)025<2374:VOTNAA>2.0.CO;2](https://doi.org/10.1175/1520-0485(1995)025<2374:VOTNAA>2.0.CO;2)
501

502 Reagan, J., Boyer, T., Schmid, C., & Locarnini, R. (2019), Subsurface Salinity [in “State of the
503 Climate in 2018”]. *Bulletin of the American Meteorological Society*, 100 (9), S79–S81,
504 <https://doi.org/10.1175/2019BAMSSStateoftheClimate.1>
505

506 Reynolds, R. W., Smith, T. M., Liu, C., Chelton, D. B., Casey, K. S. & Schlax, M. G. (2007),
507 Daily High-Resolution-Blended Analyses for Sea Surface Temperature, *Journal of Climate*, 20,
508 5473-5496, <https://doi.org/10.1175/2007JCLI1824.1>
509

510 Reynolds, R. W., Rayner, N. A., Smith, T. M., Stokes, D. C. & Wang W. (2002), An improved
511 in situ and satellite SST analysis for climate, *Journal of Climate*, 15, 1609-1625,
512 [https://doi.org/10.1175/1520-0442\(2002\)015<1609:AIISAS>2.0.CO;2](https://doi.org/10.1175/1520-0442(2002)015<1609:AIISAS>2.0.CO;2)
513

514 Roemmich, D. & Gilson, J. (2009), The 2004-2008 mean and annual cycle of temperature,
515 salinity, and steric height in the global ocean from the Argo Program, *Progress in*
516 *Oceanography*, 82, 81-100, <https://doi.org/10.1016/j.pocean.2009.03.004>
517

518 Schmeisser, L., Bond, N. A., Siedlecki, S.A., & Ackerman, T. P. (2019), The role of clouds and
519 surface heat fluxes in the maintenance of the 2013–2016 Northeast Pacific marine heatwave,
520 *Journal of Geophysical Research: Atmospheres*, 124, 10772-10783,
521 <https://doi.org/10.1029/2019JD030780>
522

523 Smale, D. A., Wernberg, T., Oliver, E. C. J., Thomsen, M., Harvey, B. P., Straub, S. C.,
524 Burrows, M. T., Alexander, L. V., Benthuyssen, J. A., Donat, M. G., Feng, M., Hobday, A. J.,
525 Holbrook, N. J., Perkins-Kirkpatrick, S. E., Scannell, H. A., Sen Gupta, A., Payne, B. L. &
526 Moore, P. J. (2019), Marine heatwaves threaten global biodiversity and the provision of
527 ecosystem services, *Nature Climate Change*, 9, 306-312, [https://doi.org/10.1038/s41558-019-](https://doi.org/10.1038/s41558-019-0412-1)
528 0412-1
529

530 Xie, L., Zheng, Q., Tian, J., Zhang, S., Feng, Y., & Yi, X. (2016), Cruise Observation of Rossby
531 Waves with Finite Wavelengths Propagating from the Pacific to the South China Sea. *Journal of*
532 *Physical Oceanography*, 46, 2897–2913, <https://doi.org/10.1175/JPO-D-16-0071.1>
533

534 Yu, L., Jin, X., Stackhouse, P. W., Wilber, A. C., Kato, S., Loeb, N. G., & Weller, R. A. (2019),
535 Global ocean heat, freshwater, and momentum fluxes [in “State of the Climate in 2018”].
536 *Bulletin of the American Meteorological Society*, 100 (9), S81–S84,
537 <https://doi.org/10.1175/2019BAMSSStateoftheClimate.1>
538

539 Zaba, K. D. & Rudnick, D. L. (2016), The 2014–2015 warming anomaly in the Southern
540 California Current System observed by underwater gliders. *Geophysical Research Letters*, 43,
541 1241-1248, <https://doi.org/10.1002/2015GL067550>
542

543 Zaba, K. D., Rudnick, D. L., Cornuelle, B. D., Gopalakrishnan, G., & Mazloff, M. R. (2020),
544 Volume and Heat Budgets in the Coastal California Current System: Means, Annual Cycles, and

545 Interannual Anomalies of 2014–16. *Journal of Physical Oceanography*, 50, 1435–1453,
546 <https://doi.org/10.1175/JPO-D-19-0271.1>